RSC Advances

PAPER

Check for updates

Phase relations, and mechanical and electronic properties of nickel borides, carbides, and nitrides from *ab initio* calculations†

Nursultan E. Sagatov, [ID] *[ab] Aisulu U. Abuova,*[b] Dinara N. Sagatova, [ID] [ac] Pavel N. Gavryushkin,[ac] Fatima U. Abuova[b] and Konstantin D. Litasov[d]

Based on density functional theory and the crystal structure prediction methods, USPEX and AIRSS, stable intermediate compounds in the Ni–X (X = B, C, and N) systems and their structures were determined in the pressure range of 0–400 GPa. It was found that in the Ni–B system, in addition to the known ambient-pressure phases, the new nickel boride, Ni_2B_3-$Immm$, stabilizes above 202 GPa. In the Ni–C system, Ni_3C-$Pnma$ was shown to be the only stable nickel carbide which stabilizes above 53 GPa. In the Ni–N system, four new phases, Ni_6N-$R\bar{3}$, Ni_3N-$Cmcm$, Ni_7N_3-$Pbca$, and NiN_2-$Pa\bar{3}$, were predicted. For the new predicted phases enriched by a light-element, Ni_2B_3-$Immm$ and NiN_2-$Pa\bar{3}$, mechanical and electronic properties have been studied.

Introduction

Transition metal borides, carbides, and nitrides are of interest in terms of materials science due to the relatively high bulk moduli, ultra-high melting points, and high chemical stabilities. This combination of properties makes these materials highly desirable for a number of industrial applications. Specifically, TMX, TMX_2, and TMX_4 (X = B, C, and N; TM-transition metal) possess comparable bulk moduli to that of superhard cubic-BN (400 GPa), such as ReB_2, WB, OsC, RuC, WC, OsN_2, PtN_2, and WN,[1–3] and some of them have been put to the test and proved to be superhard materials, such as MoN, WB_4, and FeB_4.[4–6] High pressure enables not just the production of new polymorphic modifications of known borides, carbides, and nitrides but also the synthesis of new compounds having stoichiometries not accessible at ambient pressure.[7] Therefore, recently, the number of theoretical and experimental studies devoted to the search for stable TM–X (X = B, C, and N) compounds has increased. The study of borides, carbides, and nitrides has been carried out practically for all IV group transition metals, with the exception of nickel and copper. For instance, there are many works devoted to the crystal structure predictions and high pressure syntheses of Fe–B,[6,8,9] Fe–C,[10–12] and Fe–N[13–16] compounds.

In the present paper, we investigate nickel borides, carbides, and nitrides under high pressure using modern *ab initio* crystal structure prediction methods. The Ni–B system comprises several stable (NiB, Ni_4B_3, Ni_2B, and Ni_3B) and metastable ($Ni_{23}B_6$ and Ni_7B_3) crystalline compounds.[17–19] Recently, Wang *et al.*[20] estimated the stability of ambient-pressure phases up to 100 GPa. They showed that Ni_3B and Ni_4B_3 are unstable at pressures of 80–100 GPa, while Ni_2B and NiB remains stable relative to the decomposition into isochemical mixture. In the Ni–C system, there is no stable intermediate compounds at ambient pressure. Recently, first stable nickel carbide, Ni_3C with cementite-type structure, was synthesized in a diamond anvil cell (DAC) with laser heating through a direct reaction of a nickel powder with carbon at 184 GPa.[21] In the Ni–N system, there is one known stable intermediate compound, Ni_3N, at ambient pressure. Guillaume *et al.*[22] show that the ambient-pressure structure of Ni_3N remains stable at 20 GPa. Recently, nickel pernitride (NiN_2) with marcasite-type structure was synthesized at 40 GPa using a laser-heated DAC.[23] It should be noted that no crystal structure prediction calculations were performed for these systems.

In our work, we search for new stable structures and study the phase stability, electronic and mechanical properties of the structures in the Ni–B, Ni–C, and Ni–N systems within first-principles calculations.

Computational methods

The search for new stable crystal structures of nickel borides, carbides, and nitrides were performed using evolutionary algorithms implemented in the USPEX package[24–26] and the random sampling method implemented in the AIRSS software[27,28] at 50, 100, 200, 300, and 400 GPa.

[a]Sobolev Institute of Geology and Mineralogy, Siberian Branch of the Russian Academy of Sciences, Novosibirsk 630090, Russian Federation. E-mail: sagatinho23@gmail.com
[b]L. N. Gumilyov Eurasian National University, Nur-Sultan 010008, Republic of Kazakhstan. E-mail: aisulu-us1980@yandex.ru
[c]Novosibirsk State University, Novosibirsk 630090, Russian Federation
[d]Vereshchagin Institute for High Pressure Physics, Russian Academy of Sciences, Troitsk, Moscow 108840, Russian Federation

The search with USPEX was performed in variable composition mode with 6–36 atoms per unit cell. The size of the first generation in the calculations was equal to 65 structures. 60% of the structures with the lowest enthalpy were selected after the optimization and then used to produce the next generation. A new generation was produced as follow: 35% of all structures were generated by heredity, 20% – by atomic mutation, 10%—by lattice permutation, and 35%—randomly. In average, 36–40 generations have been produced and relaxed at each pressure. Using AIRSS, about 3500–4000 structures were randomly generated and optimized for compounds with fixed stoichiometries (NiX_n; X = B, C, and N; n = 1–4) at each pressure, and those with the lowest enthalpy were selected.

The total energies and forces were calculated by solving the Schrödinger equation based on projector augmented plane-wave implementation of density functional theory (DFT) using the VASP package.[29,30] Exchange correlation effects were treated in the generalized gradient approximation (GGA) with Perdew–Bürke–Ernzerhof scheme.[31]

In all crystal structure prediction calculations, medium-quality optimization was performed using the conjugate gradient. The medium quality settings were as follows: plane-wave cutoff energy—420 eV; Monkhorst–Pack k-point sampling grid of spacing—0.5 Å^{-1}; Gaussian smearing with parameter σ = 0.15 eV. The most promising predicted structures were then optimized at various pressures with higher accuracy: the cutoff energy—700 eV, k-point sampling grid of spacing—0.2 Å^{-1}, and σ = 0.05 eV.

To investigate mechanical properties, static elastic stiffness tensor (C_{ij}) was calculated from the stress (σ) – strain (ε) relation $\sigma_i = C_{ij}\varepsilon_j$.

To investigate electronic properties, in addition to the standard PBE, Dudarev's GGA + U (ref. 32) and hybrid functional Heyd–Scuseria–Ernzerhof (HSE06)[33] methods were used.

Structures were visualized in the VESTA package,[34] and symmetries of the predicted structures were analyzed using the FindSym program.[35]

Results and discussion

Crystal structure prediction

The thermodynamic stability of the most favorable structures among the predicted ones was estimated using the convex hull diagrams, which give the convenient graphical representation of the thermodynamic stability of the predicted structures.

Crystal structure prediction calculations have been performed only for the intermediate compounds in the Ni–X (X = B, C, and N) systems. Crystal structure prediction calculations of pure Ni performed earlier by similar procedure showed its stability in $Fm\bar{3}m$ (fcc) structure up to 400 GPa.[36,37] For pure boron, carbon, and nitrogen the following data have been used: B-$R\bar{3}m$, -$Pnnm$, -$Cmca$, and -$P6_3/mcm$;[38] C-$P6_3mc$ (graphite) and -$Fd\bar{3}m$ (diamond); N-$Pa\bar{3}$, -$I2_13$,[39] -$Pba2$,[40] and -$I\bar{4}3m$.[41] The pressures of phase transition between listed polymorphic modifications are shown in Fig. 1b–3b.
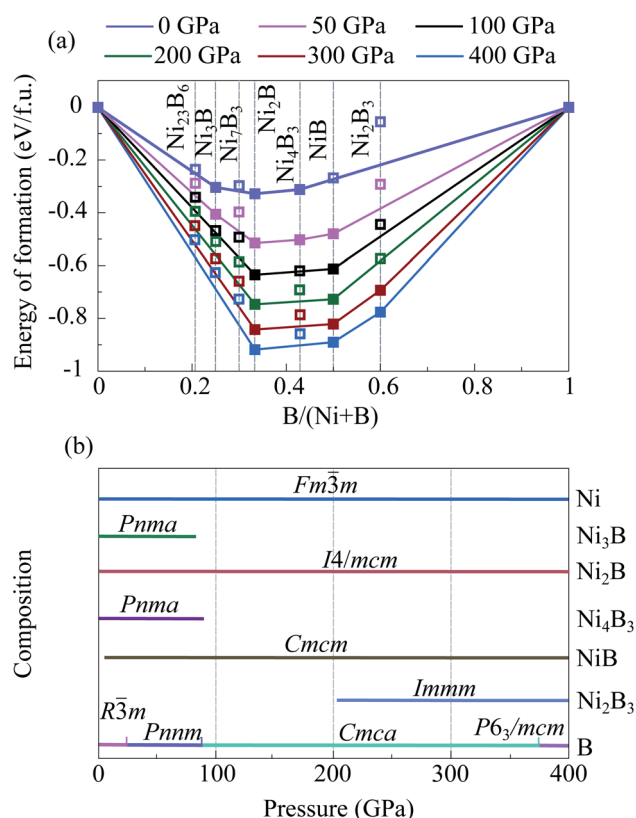

Fig. 1 Thermodynamic convex hulls of Ni−B system at various pressures and zero temperature (a). Filled symbols denote stable structures, open symbols—metastable structures. Predicted pressure–composition phase diagram for the Ni−B system (b).

Fig. 2 Stability convex hulls of the Ni−C system at various pressures and zero temperature (a). Filled symbols denote stable structures, open symbols—metastable structures. Predicted pressure–composition phase diagram for the Ni−C system (b).
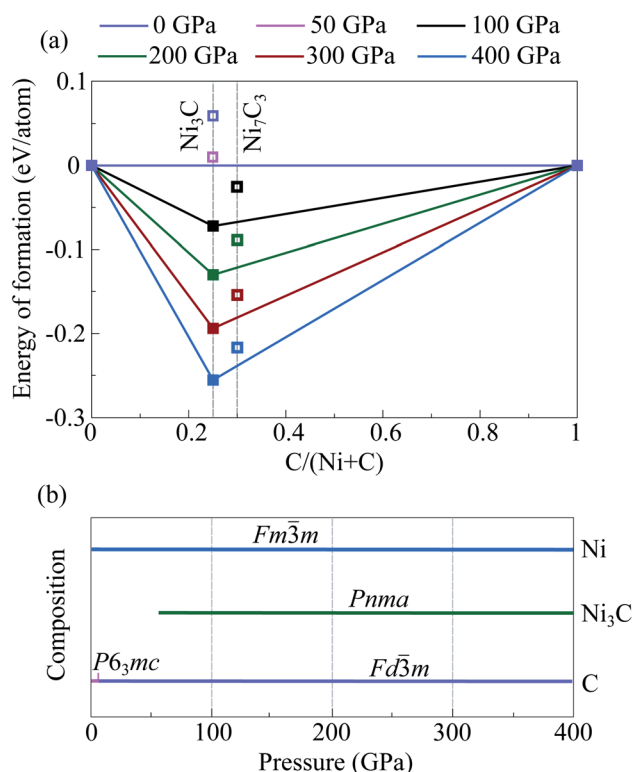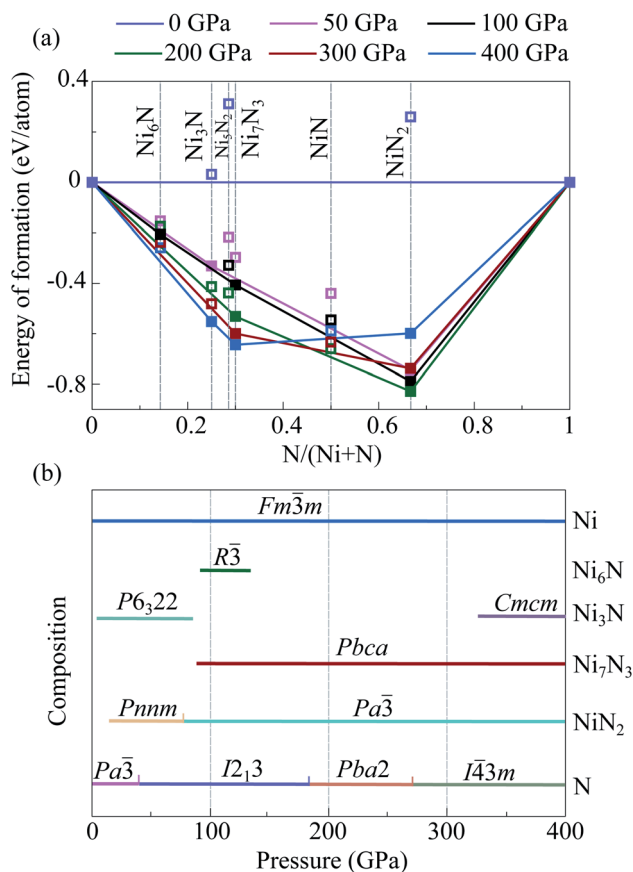
Fig. 3 Stability convex hulls of the Ni–N system at various pressures and zero temperature (a). Filled symbols denote stable structures, open symbols—metastable structures. Predicted pressure–composition phase diagram for the Ni–N system (b).

The Ni–B system. The Ni–B system is most rich in intermediate compounds with representatives in both Ni-rich and B-rich parts. In the Ni-rich part of the system four intermediate compounds, Ni_3B, Ni_2B, Ni_4B_3, and NiB, were revealed (Fig. 1a and S1†).

The Ni_3B-$Pnma$ phase was predicted at 50 GPa and it is stable from ambient pressure to 80 GPa. Above 80 GPa, Ni_3B-$Pnma$ decomposes into solid Ni and Ni_2B (Fig. 1a and Table S1†). For Ni_2B, the structure with the $I4/mcm$ symmetry was predicted at 50, 100, 200, 300, and 400 GPa as the lowest-enthalpy one. This structure is stable in the entire considered pressure range without any phase transitions (Fig. 1b). The Ni_4B_3-$Pnma$ was predicted at 50 GPa as the most energetically favorable. It is stable from 0 to 86 GPa, and above this pressure decomposes into the mixture of (Ni_2B + NiB). The NiB was predicted in the $Cmcm$ structure, which stabilizes at a pressure of 2 GPa and remains stable up to 400 GPa.

In the B-rich part of the Ni–B system, we predicted a new compound that was not previously known, namely Ni_2B_3 (Fig. 1 and Table S1†). This compound was found at 200, 300, and 400 GPa with $Immm$ symmetry. Above 202 GPa, the enthalpy of Ni_2B_3-$Immm$ becomes lower than that of mechanical mixture of ($2NiB$ + B), indicating that the Ni_2B_3-$Immm$ structure stabilizes relative to the decomposition reaction $Ni_2B_3 \leftrightarrow 2NiB + B$ (Fig. S2a†).

All these Ni–B structures are dynamically stable, which were confirmed by the calculated phonon spectra (Fig. S3†).

Although the search of the structures stable at ambient pressure has not been performed, the comparison of the found structures with the known ones show, that all the structures stable at ambient pressure, which were observed in experiments, were revealed in our calculations at 50 GPa.[42,43] In addition, we have considered $Ni_{23}B_6$,[18] observed in experiments, and Ni_7B_3 (ref. 19) suggested theoretically. According to our calculations, $Ni_{23}B_6$ is metastable at 0 GPa. This is in agreement with experimental results.[18] For Ni_7B_3, we considered two structures: Ni_7B_3-$P6_3mc$ suggested in ref. 19 and Ni_7B_3-$Pbca$ constructed from Fe_7C_3-$Pbca$,[44] replacing Fe by Ni and C by B atoms. These structures are very similar and their distinguishing by X-ray powder diffraction technique is problematic. Our calculation showed that Ni_7B_3-$Pbca$ has lower enthalpy than Ni_7B_3-$P6_3mc$ in the pressure range of 0–155 GPa (Fig. S4a†). Based on this, we suggest that most likely the $Pbca$ phase was formed in experiments of Hofmann et al.,[19] than hexagonal phase suggested in that work. With pressure increase, $Ni_{23}B_6$ and Ni_7B_3 becomes even less favorable (Fig. 1).

The Ni–C system. Crystal structure prediction calculations have revealed one stable compound in the Ni–C system, Ni_3C (Fig. 2 and Table S2†). It stabilizes in cementite-type orthorhombic structure $Pnma$, which is in agreement with recent experimental results,[21] where Ni_3C-$Pnma$ was synthesized at 184 GPa using DAC technique. According to the obtained results, Ni_3C-$Pnma$ becomes energetically more favorable than ($3Ni$ + C) above 53 GPa (Fig. 2b). There are no imaginary modes in the phonon spectra of Ni_3C-$Pnma$ (Fig. S5†), indicating that it is dynamically stable.

In addition, we constructed Ni-analogs of stable iron carbide structures Fe_7C_3-$P6_3mc$,[45] Fe_7C_3-$Pbca$,[44] and Fe_2C-$Pnma$,[12] by replacing all iron atoms by nickel ones. According to the obtained results, constructed Ni_7C_3-$Pbca$ is more favorable than constructed Ni_7C_3-$P6_3mc$ (Fig. S4b†). Nevertheless, Ni_7C_3-$Pbca$ is unstable relative to the mechanical mixtures of (Ni + C) or (Ni_3C + C) in the entire considered pressure range (Fig. 2). Similar calculations for Ni_2C-$Pnma$ showed that this compound is not stable, and the energy difference reaches 0.4 eV f.u.$^{-1}$.

Crystal structure predictions in C-rich part of the Ni–C system were performed for fixed stoichiometries, namely NiC_4, NiC_3, NiC_2, and NiC. For all these compounds the lowest-enthalpy structures are unstable and decompose into isochemical mixture in the entire considered pressure range.

The Ni–N system. The preliminary results of crystal structure prediction calculations in the Ni–N system in the pressure range of 0–300 GPa were reported as the conference proceedings.[46] Here, we extended the studied pressure range up to 400 GPa, found new structures based on the analogy with carbides and reanalyze obtained phase relations.[46] In addition to crystal structure predictions, we constructed two structural models, Ni_7N_3-$Pbca$ and Ni_7N_3-$P6_3mc$, from known iron carbides Fe_7C_3-$Pbca$ and Fe_7N_3-$P6_3mc$ by replacing all Fe by Ni atoms. The volume, lattice parameters, and atomic coordinates were optimized at various pressures for the resulting models.

Performed crystal structure prediction calculations show that there are two stable intermediate compounds in the Ni–N system at 50 GPa, Ni_3N and NiN_2 (Fig. 3 and Table S3†). Both

Table 1 Structural data of structures introduced in the present work

Compound	P (GPa)	Space group	Lattice parameters (Å, deg)			Atom	Coordinates		
							x	y	z
Ni_2B_3	250	*Immm* (#71)	a = 2.695	b = 3.357	c = 5.622	Ni1	0.000	0.000	0.804
			α = 90.00	β = 90.00	γ = 90.00	B1	0.500	0.000	0.500
						B2	0.000	0.251	0.500
Ni_6N	100	$R\bar{3}$ (#148)	a = 4.058	b = 4.058	c = 11.653	Ni1	0.316	0.331	0.246
			α = 90.00	β = 90.00	γ = 120.00	N1	0.000	0.000	0.000
Ni_7N_3	100	*Pbca* (#61)	a = 4.131	b = 12.671	c = 10.978	Ni1	−0.080	0.534	0.686
			α = 90.00	β = 90.00	γ = 90.00	Ni2	0.744	0.878	0.585
						Ni3	0.411	0.622	0.626
						Ni4	0.204	0.779	0.522
						Ni5	0.251	0.873	0.702
						Ni6	−0.092	0.718	0.693
						Ni7	0.249	−0.037	0.521
						N1	−0.004	−0.017	0.656
						N2	−0.004	0.632	0.561
						N3	0.499	0.765	0.648
Ni_3N	300	*Cmcm* (#63)	a = 2.295	b = 7.492	c = 5.541	Ni1	0.000	0.060	0.250
			α = 90.00	β = 90.00	γ = 90.00	Ni2	0.000	0.637	−0.059
						N1	0.000	0.741	0.250
NiN_2	200	$Pa\bar{3}$ (#205)	a = 4.054	b = 4.054	c = 4.054	Ni1	0.000	0.000	0.000
			α = 90.00	β = 90.00	γ = 90.00	N1	0.592	0.592	0.592

predicted Ni_3N-$P6_322$ and NiN_2-*Pnnm* were observed earlier in high-pressure experiments.[22,23] According to obtained results, Ni_3N-$P6_322$ is stable in the pressure range of 4–96 GPa. Below 4 GPa, Ni_3N-$P6_322$ is unstable relative to mechanical mixture of (3Ni + N), and above 96 GPa it is unstable relative to mechanical mixture of (Ni_7B_3 + Ni). NiN_2-*Pnnm* stabilizes above 14 GPa. At 100 GPa, there are three stable nickel nitrides, predicted Ni_6N-$R\bar{3}$ and NiN_2-$Pa\bar{3}$, and constructed Ni_7N_3-*Pbca*. Ni_6N-$R\bar{3}$ stabilizes at 98 GPa, and above 114 GPa decomposes into solid Ni and Ni_7N_3. Constructed Ni_7N_3-*Pbca* is more favorable than constructed Ni_7N_3-$P6_3mc$ in the entire pressure range (Fig. S2†). Ni_7N_3-*Pbca* become stable relative to Ni_3N + NiN_2 above 93 GPa and stable at least up to 400 GPa. NiN_2 undergoes a phase transition from known NiN_2-*Pnnm* to the new predicted NiN_2-$Pa\bar{3}$ at 96 GPa. NiN_2-$Pa\bar{3}$ is stable at least up to 400 GPa. At 400 GPa, in addition to Ni_7N_3-*Pbca* and NiN_2-$Pa\bar{3}$, one new nitride Ni_3N-*Cmcm* was predicted. It stabilizes relative to the mechanical mixture of (Ni_7N_3 + Ni) above 331 GPa. Phonon calculations show that the predicted nickel nitrides are dynamically stable; *i.e.*, they have no imaginary modes in the phonon spectra (Fig. S6†).

Crystal chemistry of the predicted structures

Structural data of the new predicted compounds are given in Table 1.

The most crystallochemically interesting structures are the structures of compounds enriched by the light element. We have revealed two such compounds, NiN_2 and Ni_2B_3. Two found structures of NiN_2, NiN_2-$Pa\bar{3}$, corresponds to the well-known structural type of pyrite with N–N molecular units.

The crystal structure of Ni_2B_3 is also characterised by the covalently bonded units. In this case, these are infinite (001) layers of boron atoms. In the layer each B atom is connected to

four other B atoms forming the net with hexagonal and rhombic loops (Fig. 4a). The B–B bond distance within the layer is 1.67 Å at 250 GPa. The elemental boron is characterised by nearly the same B–B distance, 1.7 Å. The covalent nature of B–B bond in Ni_2B_3 structure is also confirmed by the electronic density distribution (Fig. S8†). Boron layers alternates with layers of Ni atoms, forming rectangular centered network (Fig. 4b). Each Ni is coordinated by 10 boron atoms, the six of which are from the top, and four are from the bottom layer. The performed analysis of the structures with the similar stoichiometry has revealed another structure, W_2CoB_2, belonging to the described structural type.[47,48]

Graphical representation of the Ni_6N-$R\bar{3}$, Ni_3N-*Cmcm*, Ni_7N_3-*Pbca*, and NiN_2-$Pa\bar{3}$ crystal structures are shown in Fig. S7.†

Elastic properties

Transition metal borides, carbides, and nitrides often exhibit extraordinary mechanical properties. Elastic constants are helpful to understand the mechanical properties and provide
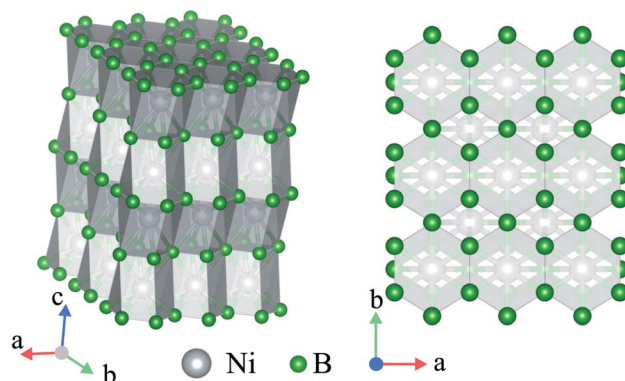

Fig. 4 Crystal structure of Ni_2B_3-*Immm* in two projections.

Table 2 Calculated elastic constants C_{ij} (GPa) of NiN$_2$-$Pa\bar{3}$ and Ni$_2$B$_3$-$Immm$ at different pressures

Phase	P (GPa)	C_{11}	C_{12}	C_{13}	C_{22}	C_{23}	C_{33}	C_{44}	C_{55}	C_{66}
NiN$_2$-$Pa\bar{3}$	100	1311.6	326.4	326.2	1311.5	326.5	1311.6	204.8	204.8	204.8
	200	1887.7	609.7	609.5	1887.7	609.7	1887.7	243.5	243.5	243.5
	300	2363.3	891.5	891.3	2363.3	891.5	2363.3	263.1	263.1	263.1
	400	2787.9	1175.5	1175.2	2787.9	1175.5	2787.9	272.8	272.8	272.8
Ni$_2$B$_3$-$Immm$	200	1372.3	831.2	724.6	1354.5	774.6	1429.9	305.3	169.8	493.4
	300	1773.5	1114.3	973.2	1750.0	1045.2	1895.3	400.4	239.6	643.6
	400	2153.0	1389.9	1218.3	2126.0	1307.1	2336.1	486.2	297.1	780.4
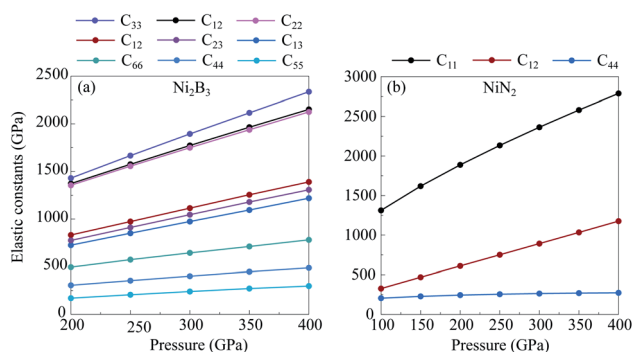
Fig. 5 Calculated elastic constants of Ni$_2$B$_3$-$Immm$ (a) and NiN$_2$-$Pa\bar{3}$ (b) as functions of pressure.

useful information to estimate the hardness of a structure. To that end, we investigate the elastic properties of new predicted compounds enriched by a light-element, NiN$_2$-$Pa\bar{3}$ and Ni$_2$B$_3$-$Immm$, within the strain–stress method in combination with the DFT. Calculated elastic constants of NiN$_2$-$Pa\bar{3}$ and Ni$_2$B$_3$-$Immm$ are listed in Table 2. From Table 2 and Fig. 5, it could be seen that the elastic constants C_{ij} for these structures are all positive, increase monotonically with increasing pressure, and the whole set of the elastic constants of the structures satisfy the mechanical stability criteria.[49] This means that NiN$_2$-$Pa\bar{3}$ and Ni$_2$B$_3$-$Immm$ are mechanically stable in the considered pressure range.

Calculated bulk modulus B of NiN$_2$-$Pa\bar{3}$ and Ni$_2$B$_3$-$Immm$ are ~87% and ~82% of that estimated for diamond, respectively, while shear modulus G of NiN$_2$-$Pa\bar{3}$ and Ni$_2$B$_3$-$Immm$ are ~35%

and ~38% of that estimated for diamond, respectively (Table 3). Predicted NiN$_2$-$Pa\bar{3}$ and Ni$_2$B$_3$-$Immm$ are ductile materials since their B/G values (Table 3) are greater than 1.75.[50]

In order to investigate the hardness of NiN$_2$-$Pa\bar{3}$ and Ni$_2$B$_3$-$Immm$ at various pressures we employ empirical Chen[51] and Tian et al.[52] models. The Vickers hardness of NiN$_2$-$Pa\bar{3}$ and Ni$_2$B$_3$-$Immm$ are estimated to be 19 GPa and 12 GPa, respectively. The hardness of NiN$_2$-$Pa\bar{3}$ decreases with increasing pressure, while that of Ni$_2$B$_3$-$Immm$ increases with increasing pressure. The estimated H_V of both predicted structures are below minimal criteria of 20 GPa of hardness. Therefore, NiN$_2$-$Pa\bar{3}$ and Ni$_2$B$_3$-$Immm$ are not classified as a hard materials.

Electronic structure

To investigate electronic characteristics of NiN$_2$-$Pa\bar{3}$ and Ni$_2$B$_3$-$Immm$, we calculate their total/partial electronic density of states (DOS) (Fig. 6) and band structures (Fig. 7).

The Fermi level of the considered phases is set to zero. The result shows that Ni$_2$B$_3$-$Immm$ exhibit metallic features. From calculated partial DOS (Fig. 6a), we noticed that Ni d orbital has hybridization with B p orbital. The lower bands in the valence band region are mainly contributed by B 2p states, while near the top of valence bands main contributors are Fe 3d states. The Fermi level are mostly occupied by the Fe 3d electrons, with some contribution of B 2p electrons. On the other hand, NiN$_2$-$Pa\bar{3}$ is found to be a semiconductor with the indirect band gap of 1.297 eV. The electronic states at the lower energy range of

Table 3 Calculated bulk modulus B (GPa), shear modulus G (GPa), the B/G ratio and Vickers hardness (GPa) of NiN$_2$-$Pa\bar{3}$ and Ni$_2$B$_3$-$Immm$ at different pressures. For comparison, the data[53] on diamond are presented

Phase	P (GPa)	B	G	B/G	H_V^{Chen}	H_V^{Tian}
NiN$_2$-$Pa\bar{3}$	100	654.8	293.6	2.23	18.7	20.6
	200	1035.7	362.7	2.86	15.4	18.1
	300	1382.1	403.2	3.43	12.8	15.8
	400	1712.9	428.6	4.00	10.7	13.9
Ni$_2$B$_3$-$Immm$	200	979.7	297.5	3.29	10.9	13.4
	300	1298.1	388.1	3.34	12.9	15.9
	400	1604.8	467.7	3.43	14.2	17.6
Diamond[53]	100	838	848	—	—	—
	200	1188	1023	—	—	—
	300	1521	1168	—	—	—
	400	1839	1295	—	—	—

Fig. 6 Total and partial DOS calculated for Ni$_2$B$_3$-$Immm$ (a) and NiN$_2$-$Pa\bar{3}$ (b).
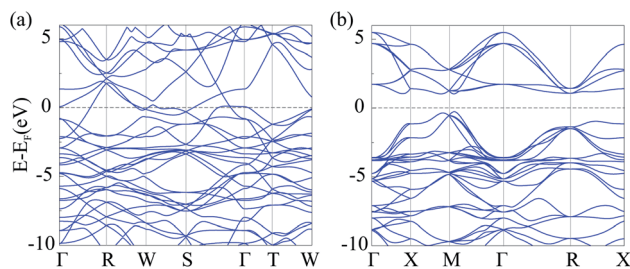
Fig. 7 Calculated band structures of Ni_2B_3-*Immm* (a) and NiN_2-*Pa$\bar{3}$* (b).

various planes and different colours indicate diverse degrees of electron localization: the red means that the electron is totally localized at the realm and blue means the opposite situation, namely, the electron is not localized at all. According to the obtained result, in Ni_2B_3-*Immm*, we could observe that the boron atoms form a mesh structure. In NiN_2-*Pa$\bar{3}$*, the nitrogen atoms form N_2 dimers. In both structures, valence electrons are not localized around the Ni atoms. These data suggest that the chemical bonds among nickel mainly exhibit ionic characteristics and boron/nitrogen atoms form covalent chemical bonds, which seemingly do not strongly interact with nickel atoms.

the valence bands are mainly contributed by N 2p orbitals, while Ni 3d orbitals dominate at the top of valence bands. The main contributors in the conduction band region are unoccupied Fe 3d states, with some contribution of N 2p states.

It is well-known that GGA often underestimates the width of band gap. For this reason, and also to avoid misleading, we performed GGA + U (with U = 2, 4 eV) and hybrid (HSE06) calculations. The obtained results showed that PBE, GGA + U, and HSE06 give qualitatively the same DOS and band structures (Fig. S9 and S10†). This fact indicates that the results obtained by standard PBE calculations are valid. For NiN_2-*Pa$\bar{3}$*, the band gap obtained by GGA + U with U = 2 eV was equal to 1.524 eV, by GGA + U with U = 4 – 1.001 eV, by HSE06 − 2.237 eV (Fig. S10b†).

To elucidate chemical bond properties of Ni_2B_3-*Immm* and NiN_2-*Pa$\bar{3}$*, electron localization function (ELF) diagrams were constructed (Fig. 8). The ELFs of the structures are derived from

Conflicts of interest

There are no conflicts to declare.

Acknowledgements

Notes and references

1 J. C. Crowhurst, A. F. Goncharov, B. Sadigh, C. L. Evans, P. G. Morrall, J. L. Ferreira and A. J. Nelson, *Science*, 2006, **311**, 1275–1278.

2 Z. Zhao, L. Xu, L.-M. Wang, B. Xu, M. Wang, Z. Liu and J. He, *Comput. Mater. Sci.*, 2011, **50**, 1592–1596.

3 Y. Zhang, Z.-R. Liu, D.-W. Yuan, Q. Shao, J.-H. Chen, C.-L. Wu and Z.-L. Zhang, *Acta Metall. Sin.*, 2019, **32**, 1099–1110.

4 M. Ürgen, O. Eryilmaz, A. Çakir, E. Kayali, B. Nilüfer and Y. Işik, *Surf. Coat. Technol.*, 1997, **94–95**, 501–506.

5 R. Mohammadi, A. T. Lech, M. Xie, B. E. Weaver, M. T. Yeung, S. H. Tolbert and R. B. Kaner, *Proc. Natl. Acad. Sci. U. S. A.*, 2011, **108**, 10958–10962.

6 H. Gou, N. Dubrovinskaia, E. Bykova, A. A. Tsirlin, D. Kasinathan, W. Schnelle, A. Richter, M. Merlini, M. Hanfland, A. M. Abakumov, D. Batuk, G. Van Tendeloo, Y. Nakajima, A. N. Kolmogorov and L. Dubrovinsky, *Phys. Rev. Lett.*, 2013, **111**, 157002.

7 A. Zerr, R. Riedel, T. Sekine, J. E. Lowther, W.-Y. Ching and I. Tanaka, *Adv. Mater.*, 2006, **18**, 2933–2948.

8 I. Harran, H. Wang, Y. Chen, M. Jia and N. Wu, *J. Alloys Compd.*, 2016, **678**, 109–112.

9 A. N. Kolmogorov, S. Shah, E. R. Margine, A. F. Bialon, T. Hammerschmidt and R. Drautz, *Phys. Rev. Lett.*, 2010, **105**, 217003.

10 Z. G. Bazhanova, A. R. Oganov and O. Gianola, *Phys.-Usp.*, 2012, **55**, 489.

11 G. L. Weerasinghe, R. J. Needs and C. J. Pickard, *Phys. Rev. B: Condens. Matter Mater. Phys.*, 2011, **84**, 174110.
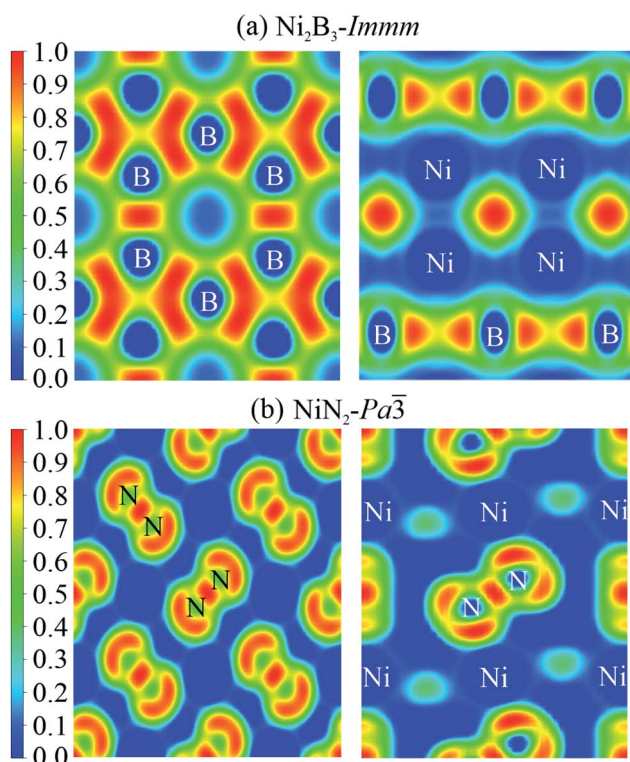
Fig. 8 Electron localization functions of Ni_2B_3-*Immm* (a) and NiN_2-*Pa$\bar{3}$* (b).

© 2021 The Author(s). Published by the Royal Society of Chemistry

12 N. Sagatov, P. Gavryushkin, I. Medrish, T. Inerbaev and K. Litasov, *Russ. Geol. Geophys.*, 2020, **61**, 1345–1353.

13 L. Wu, R. Tian, B. Wan, H. Liu, N. Gong, P. Chen, T. Shen, Y. Yao, H. Gou and F. Gao, *Chem. Mater.*, 2018, **30**, 8476–8485.

14 Y. Chen, X. Cai, H. Wang, H. Wang and H. Wang, *Sci. Rep.*, 2018, **8**, 10670.

15 Z. Wang, Y. Li, H. Li, I. Harran, M. Jia, H. Wang, Y. Chen, H. Wang and N. Wu, *J. Alloys Compd.*, 2017, **702**, 132–137.

16 M. Bykov, E. Bykova, G. Aprilis, K. Glazyrin, E. Koemets, I. Chuvashova, I. Kupenko, C. McCammon, M. Mezouar, V. Prakapenka, *et al.*, *Nat. Commun.*, 2018, **9**, 2756.

17 V. Raghavan, *J. Phase Equilib. Diffus.*, 2007, **28**, 377–379.

18 M. Baricco, E. Ferrari and L. Battezzati, *MRS Proceedings*, 1995, **398**, 81.

19 K. Hofmann, N. Kalyon, C. Kapfenberger, L. Lamontagne, S. Zarrini, R. Berger, R. Seshadri and B. Albert, *Inorg. Chem.*, 2015, **54**, 10873–10877.

20 M. Wang, J. Xie, K. Xue and L. Li, *Comput. Mater. Sci.*, 2021, **194**, 110465.

21 T. Fedotenko, S. Khandarkhaeva, L. Dubrovinsky, K. Glazyrin, P. Sedmak and N. Dubrovinskaia, *Minerals*, 2021, **11**, 516.

22 C. Guillaume, J. P. Morniroli, D. J. Frost and G. Serghiou, *J. Phys.: Condens. Matter*, 2006, **18**, 8651–8660.

23 K. Niwa, R. Fukui, T. Terabe, T. Kawada, D. Kato, T. Sasaki, K. Soda and M. Hasegawa, *Eur. J. Inorg. Chem.*, 2019, **2019**, 3753–3757.

24 A. R. Oganov and C. W. Glass, *J. Chem. Phys.*, 2006, **124**, 244704.

25 A. R. Oganov, A. O. Lyakhov and M. Valle, *Acc. Chem. Res.*, 2011, **44**, 227–237.

26 A. O. Lyakhov, A. R. Oganov, H. T. Stokes and Q. Zhu, *Comput. Phys. Commun.*, 2013, **184**, 1172–1182.

27 C. J. Pickard and R. J. Needs, *Phys. Rev. Lett.*, 2006, **97**, 045504.

28 C. J. Pickard and R. J. Needs, *J. Phys.: Condens. Matter*, 2011, **23**, 053201.

29 G. Kresse and J. Furthmüller, *Phys. Rev. B: Condens. Matter Mater. Phys.*, 1996, **54**, 11169–11186.

30 G. Kresse and J. Furthmüller, *Comput. Mater. Sci.*, 1996, **6**, 15–50.

31 J. P. Perdew, K. Burke and M. Ernzerhof, *Phys. Rev. Lett.*, 1996, **77**, 3865.

32 S. L. Dudarev, G. A. Botton, S. Y. Savrasov, C. J. Humphreys and A. P. Sutton, *Phys. Rev. B: Condens. Matter Mater. Phys.*, 1998, **57**, 1505–1509.

33 J. Heyd, G. E. Scuseria and M. Ernzerhof, *J. Chem. Phys.*, 2003, **118**, 8207–8215.

34 K. Momma and F. Izumi, *J. Appl. Crystallogr.*, 2011, **44**, 1272–1276.

35 H. T. Stokes and D. M. Hatch, *J. Appl. Crystallogr.*, 2005, **38**, 237–238.

36 T. M. Inerbaev, N. Sagatov, D. Sagatova, P. N. Gavryushkin, A. T. Akilbekov and K. D. Litasov, *ACS Earth Space Chem.*, 2020, **4**, 1978–1984.

37 N. E. Sagatov, A.-D. B. Bazarbek, T. M. Inerbaev, P. N. Gavryushkin, A. T. Akilbekov and K. D. Litasov, *ACS Earth Space Chem.*, 2021, **5**, 596–603.

38 H. Dong, A. R. Oganov, V. V. Brazhkin, Q. Wang, J. Zhang, M. M. D. Esfahani, X.-F. Zhou, F. Wu and Q. Zhu, *Phys. Rev. B*, 2018, **98**, 174109.

39 M. I. Eremets, A. G. Gavriliuk, I. A. Trojan, D. A. Dzivenko and R. Boehler, *Nat. Mater.*, 2004, **3**, 558–563.

40 Y. Ma, A. R. Oganov, Z. Li, Y. Xie and J. Kotakoski, *Phys. Rev. Lett.*, 2009, **102**, 065501.

41 C. J. Pickard and R. Needs, *Phys. Rev. Lett.*, 2009, **102**, 125702.

42 R. Gumeniuk, H. Borrmann and A. Leithe-Jasper, *Z. Kristallogr. - New Cryst. Struct.*, 2006, **221**, 425–426.

43 E. Havinga, H. Damsma and P. Hokkeling, *J. Less-Common Met.*, 1972, **27**, 169–186.

44 C. Prescher, L. Dubrovinsky, E. Bykova, I. Kupenko, K. Glazyrin, A. Kantor, C. McCammon, M. Mookherjee, Y. Nakajima, N. Miyajima, *et al.*, *Nat. Geosci.*, 2015, **8**, 220–223.

45 N. Sagatov, P. N. Gavryushkin, T. M. Inerbaev and K. D. Litasov, *RSC Adv.*, 2019, **9**, 3577–3581.

46 P. N. Gavryushkin, N. Sagatov, D. Sagatova, M. V. Banaev, K. G. Donskikh and K. D. Litasov, *J. Phys.: Conf. Ser.*, 2020, **1590**, 012010.

47 E. Partee and B. Chabot, *Handb. Phys. Chem. Rare Earths*, 1984, **6**, 113–334.

48 M. Pani, F. Merlo and M. L. Fornasini, *Z. Kristallogr. - Cryst. Mater.*, 2002, **217**, 415–419.

49 Z. Wu, E. Zhao, H. Xiang, X. Hao, X. Liu and J. Meng, *Phys. Rev. B: Condens. Matter Mater. Phys.*, 2007, **76**, 054115.

50 S. Pugh, *London, Edinburgh Dublin Philos. Mag. J. Sci.*, 1954, **45**, 823–843.

51 X.-Q. Chen, H. Niu, D. Li and Y. Li, *Intermetallics*, 2011, **19**, 1275–1281.

52 Y. Tian, B. Xu and Z. Zhao, *Int. J. Refract. Met. Hard Mater.*, 2012, **33**, 93–106.

53 E. Güler and M. Güler, *Chin. J. Phys.*, 2015, **53**, 195–205.